Accepted Manuscript

Enhanced thermoelectric performance of twisted bilayer graphene nanoribbons junction

Shuo Deng, Xiang Cai, Yan Zhang, Lijie Li

PII:	S0008-6223(19)30092-2
DOI:	10.1016/j.carbon.2019.01.089
Reference:	CARBON 13893
To appear in:	*Carbon*
Received Date:	07 November 2018
Accepted Date:	25 January 2019

Please cite this article as: Shuo Deng, Xiang Cai, Yan Zhang, Lijie Li, Enhanced thermoelectric performance of twisted bilayer graphene nanoribbons junction, *Carbon* (2019), doi: 10.1016/j.carbon.2019.01.089

Enhanced thermoelectric performance of twisted bilayer graphene nanoribbons junction

Shuo Deng[1,2], Xiang Cai[2], Yan Zhang[3*], and Lijie Li[2*]
[1]School of Logistic Engineering, Wuhan University of Technology, Wuhan 430070
[2]College of Engineering, Swansea University, Swansea SA1 8EN
[3]School of Physics, University of Electronic Science and Technology of China, Chengdu 610054
*Emails: zhangyan@uest.edu.cn, L.Li@swansea.ac.uk

Abstract

We investigate the electron transport and thermoelectric property of twisted bilayer graphene nanoribbon junction (TBGNRJ) in 0°, 21.8°, 38.2° and 60° rotation angles by first principles calculation with Landauer-Buttiker and Boltzmann theories. It is found that TBGNRJs exhibit a strong reduction of thermal conductance compared with the single graphene nanoribbon (GNR) and negative differential resistance (NDR) in 21.8 ° and 38.2 ° rotation angles under ± 0.2 V bias voltage. More importantly, three peak ZT values of 2.0, 2.7 and 6.1 can be achieved in the 21.8° rotation angle at 300K. The outstanding ZT values of TBGNRJs are interpreted as the combination of the reduced thermal conductivity and enhanced electrical conductivity at optimized angles.

1 Introduction

Graphene is the first true 2-dimensional (2D) material, which consists of carbon atoms forming regular hexagonal lattice[1]. In the prior research, many outstanding properties of graphene were discovered, such as high electrical conductivity and carrier mobility[2-6], high thermal conductivity[7], and superior mechanical properties[8, 9]. Hence graphene can have many applications in electronic and mechanical devices. In particular, it has been applied in thermoelectric devices[10, 11]. The energy conversion efficiency of thermoelectric materials can be described by the figure of merit $ZT = S^2 G_e T/(\kappa_e + \kappa_{ph})$, where the G_e, S and T are the electrical conductance, Seebeck coefficient and temperature, respectively. κ_e and κ_{ph} are the heat transport coefficient of electrons and phonons. A good thermoelectric material should have a high electrical conductivity, Seebeck coefficient and low thermal conductivity. On one hand, the Dirac-cone band structure of graphene makes it to display a high electrical conductivity[5, 6]. On the other hand, the thermoelectric performance of graphene is poor because of its high thermal conductivity, and the closed bandgap which leads to a small Seebeck coefficient[12]. As a result, the key to improve the ZT of graphene devices is find a trade-off between the Seebeck coefficient, electrical conductance and heat transport coefficient. In prior studies, the specially designed nanostructured graphene can have increased Seebeck coefficient and suppressed heat transport coefficient without greatly reducing electrical conductance due to the quantum confinement effect[10, 13, 14]. In these graphene devices, graphene nanoribbons

(GNRs) has demonstrated better thermoelectric performances as the Seebeck coefficient and *ZT* value can be increased by the finite size effect[15-18]. One of earlier attempts on the thermoelectric performance of GNRs was reported by Ouyang *et al*[18]. They found that a higher Seebeck coefficient in GNRs compared with the pristine graphene is attributed to the edge geometry of GNRs, which plays an important role in enhancing the thermoelectric performance. In 2012, Jin *et al* reported that the armchair GNR exhibits a higher *ZT* value than zigzag GNRs, and *ZT* value increases with the decrease of the GNRs width[15]. A chevron type edge GNR was proposed demonstrating a *ZT* value of 3.25 at 800 K[19]. Nguyen *et al* discovered that the thermal conductance in the bilayer GNRs is hundreds times weaker than the pristine graphene because the weak van der Waals (vdW) interaction between two layers[20]. In recent several years, in order to improve thermoelectric performance of GNRs, different schemes based on more sophisticated GNR nanostructures have been designed [21, 22], such as using boundary effect[16, 23, 24], interface effect[25], doping[17, 26], and structure defect or wrinkles[27-30].

Bilayer graphene structures with optimized twisting angles aiming to achieve much improved performances such as high temperature superconductivity and strong interlayer coupling have been theoretically and experimentally investigated recently [31-34]. Because the bilayer graphene structure efficiently limits the thermal conductivity in the normal direction to the 2D plane attributed to the vdW force[20], this will lead to a new approach to further increase the thermoelectric performance.

In this work, the electron transport and thermoelectric performance of twisted bilayer graphene nanoribbon junction (TBGNRJs) in 0 °, 21.8 °, 38.2 ° and 60 ° rotation angles are systematically researched using the first principles method, which has been applied in previous studies on GNR junctions[20, 35]. It is discovered that that TBGNRJs exhibit negative differential resistance (NDR) in 21.8 ° and 38.2 ° rotation angles under ± 0.2 *V* bias voltage. Moreover, *ZT* values of 2.0, 2.7 and 6.1 can be achieved at different chemical potentials for the 21.8 ° rotation angle at 300K.

2 Computational procedure

The theoretical simulation of the twisted bilayer graphene structures starts with the Generalized Lattice Match (GLM) method, which is for investigating the relationship between the mismatch strain and the number of atoms[36]. The optimization of twisting angles is conducted by using the balanced mismatch strain and number of atoms, it is targeted to have a lower mismatch strain and at the same time a smaller number of atoms. As shown in the Figure 1(a) and (b), the vectors $\mathbf{v}_1$ and $\mathbf{v}_2$ defined the surface cell of the bottom graphene layer while the vectors $\mathbf{u}_1$ and $\mathbf{u}_2$ as the surface cell of the top graphene layer. The relationship between [$\mathbf{v}_1$, $\mathbf{v}_2$] and [$\mathbf{u}_1$, $\mathbf{u}_2$] is expressed as $\mathbf{A}[\mathbf{u}_1, \mathbf{u}_2] = [\mathbf{v}_1, \mathbf{v}_2]$, where **A** is the affine transformation matrix. The rotation matrix **U** has a form as[36].

$$\mathbf{U} = \begin{bmatrix} \cos(\phi) & -\sin(\phi) \\ \sin(\phi) & \cos(\phi) \end{bmatrix} \quad (1)$$

$$\phi = |\phi_a - \phi_b|/2 \quad (2)$$

$$\mathbf{P} = \boldsymbol{U}^{\boldsymbol{T}}\mathbf{A} \tag{3}$$

where, ϕ is the twisting angle of bilayers graphene, ϕ_a is the angle between the vectors $\mathbf{u}_1$ and $\mathbf{u}_2$, ϕ_b is the angle between the vectors $\mathbf{v}_1$ and $\mathbf{v}_2$, matrix $\mathbf{P}$ defines the 2D strain tensor for deforming one cell into the other. We only calculate the twisting angles from 0 º to 60 º because the crystal structure of graphene is a regular hexagon. In order to sustain the structural stability and avoid having a large size cell, we analyzed the twisting angles of 0 º, 21.8 º, 38.2 º and 60 º, at which the strain of lattice mismatch is calculated to be 0%. Previous studies have shown that AA (0 º rotation angle) and AB (60 º rotation angle) stacking of bilayer graphene are the most common stacking style in the research [37]. The other twisting angles (21.8 º and 38.2 º) were chosen, because they had a small size of cell comparing with other rotation angles.

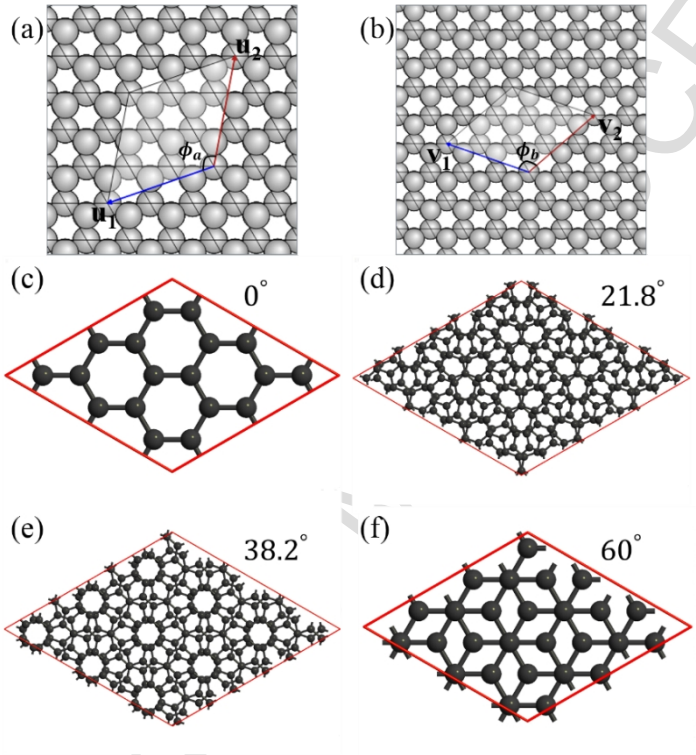

Figure 1. The surface cell of top (a) and bottom of graphene (b). (c)-(f) show the top view of the atomic arrangement of the twisted bilayer graphene with 0 º, 21.8 º, 38.2 º and 60 º rotation angles, respectively.

All the modelling and calculations have been implemented by the Quantum Atomistix ToolKit (ATK2018) simulation tools[38]. Calculations of the electronic properties have been performed within the framework of density functional theory (DFT). In the geometry optimization, we use the semi-empirical corrections by the Grimme DFT-D2 model to calculate the distance between two layers, which accounts the long-range vdW interaction [39]. The structure is fully relaxed until the force on each atom becomes smaller than 0.01 eV/Å. The generalized gradient approximation (GGA) with the parametrization of Perdew-Burke-Ernzerhof (PBE), cut-off energy of 150 Ry and 12×12×1 k-points grid were used. To avoid the interaction of the periodic boundary conditions, a large vacuum spacing of at least 25 Å is added along the normal direction to the electrons transport plane. In our transmission calculation, the device model is divided into central part, left and right electrodes. The Brillouin zone of the junction is sampled by a 1×1×100 *k*-mesh and a double-zeta polarized for all atoms.

The electronic and phonon transmissions are calculated by the nonequilibrium Green function method and molecular dynamics method, respectively. The calculated rotation angle (θ), lattice constant (a), mean absolute strain (ε) and surface distance between two layers (d) are listed in Table 1. For AA (0 ° rotation angle) and AB (60 ° rotation angle) stacking structures of bilayer graphene, the interface distance is 3.35 Å, which is close to those of the same bilayer graphene structures in references[40, 41]. As shown in Figure 2, the fat band structures and projected shells for four twisted bilayer graphene cells have been calculated along the path through *Γ*-*M*-*K*-*Γ*. The energy bands originated from the *s*, *p* and *d* orbitals are marked by red, blue and green lines, respectively. We obtained two Dirac cones around the *K*-point originated from *p* orbital because the band splitting occurs when two graphene layers interact. The splitting between the bands in the Dirac cones is responsible for low-dispersion bands near the *M* point[41, 42]. Although the top views of the atomic arrangement of the twisted bilayer graphene cells (Figure 1) look different, the band structures calculated for the rotation angles 0° and 60° seem very similar, the same for the rotation angles 21.8° and 38.2°. It is because that the crystal structure of graphene is a regular hexagon, which has rotational symmetry. The 0° and 60° (21.8° and 38.2°) are two sets of rotational symmetry angles. The similarity of band structures with rotational symmetry angles were described in reference [43].

Table 1. Rotation angle (θ), lattice constant (a), mean absolute strain (ε), and surface distance between two layers (d) for bilayer graphene.

θ (°)	a (Å)	ε	d (Å)
0	2.46	0%	3.35
21.8	6.51	0%	3.25
38.2	6.51	0%	3.25
60	2.46	0%	3.35

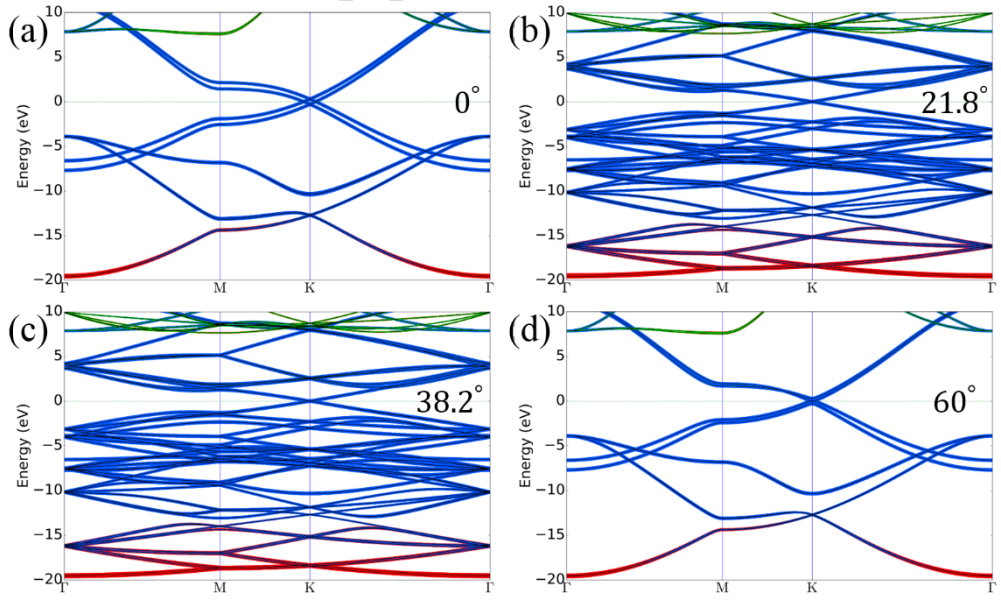

Figure 2. The computed fat band structures and projected shells of bilayer graphene structures with 0 ° (a) 21.8 ° (b), 38.2 ° (c) and 60 ° (d) rotation angles.

Based on these twisted bilayer graphene structures, overlapped TBGNRJs has been devised, followed by the investigation on electron transport and thermoelectric performance. Figure 3 shows the details of the device model, which is divided into central scattering region (SR), left electrode (LE) and right electrode (RE). The length of the overlap region in the TBGNRJs is 5 unit-cells along the transport direction, which is the minimum length that avoids modelling imperfectness, i.e. length shorter than 5 unit-cells will result in overlapped part entering to the electrode extension region. With the increase of the overlap length, the interlayer coupling enhances, which leads to increase of thermal conductance and reduction of *ZT*, which is consistent with the prior reference [20]. Moreover, models with longer overlap regions take much longer time to compute.

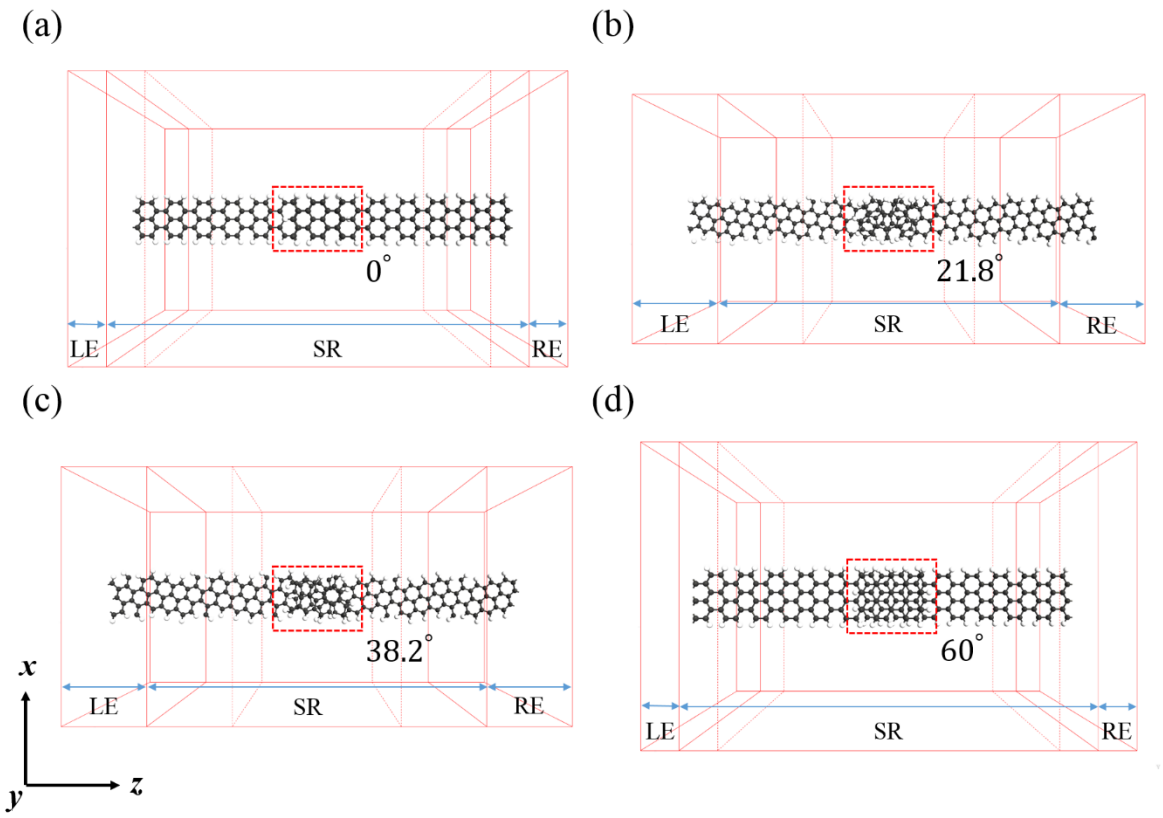

Figure 3. The top view of the 0 º (a) 21.8 º (b), 38.2 º (c) and 60 º (d) TBGNRJs.

3 Results and discussion

First, we investigate the *I-V* characteristics of these TBGNRs. The current across a TBGNR can be calculated from the Landauer-Buttiker equation[44]:

$$I = \frac{e}{h}\int dE\left(f_L(E) - f_R(E)\right)T_e(E) \qquad (4)$$

Where, $T_e(E) = Tr\left[t^+ t\right](E)$ is the total electron transmission, $f_R(E)$ and $f_L(E)$ are the Fermi distribution functions of the right and left electrode, respectively.

Figure 4(a) shows the calculated current as a function of the bias voltage for the TBGNRJs in 0 º, 21.8 º, 38.2 º and 60 º rotation angles. With the increase of the bias voltage, the current

displays an increasing trend. Moreover, the *I-V* curves of 0 ° exhibit a behavior similar to a back-to-back p-n junction. However, it is not the case for the 60 ° TBGNRJ where the *I-V* curve exhibits transistor-like behavior. Similar results were shown in a prior publication[40]. We calculated the *I-V* curves with different widths for 0 ° and 60 ° TBGNRJs in Figure 4(c) and (d). For two graphene cells width, the *I-V* curves of 0 ° and 60 ° TBGNRJs show back-to-back p-n junction and transistor behavior, respectively. However, with the increase of the width, the shape of *I-V* curves changed, which means that the electronic transport properties of graphene nanoribbons strongly depend on their width [45]. Because of connecting only the top layer to the left electrode and bottom layer to the right electrode, the current flowing through the interface depends on the coupling between bilayers. For 0 ° and 60 ° rotation angles, different interlayer angles induce different interlayer coupling and electronic transport, which causes various development trends of *I-V* curves. At 21.8 ° and 38.2 ° rotation angles, the *I-V* and *dI*/*dV* curves (Figure 4(b)) are asymmetric, which is due to the non-central symmetric structure in the twisted junctions. Under the 1 *V* bias voltage, the current intensity of 21.8 ° TBGNRJ is higher than 38.2 ° TBGNRJ, while this relationship reverses at the -1 *V* bias voltage. Under the 0 ° and 60 ° rotation angles, the *I-V* and *dI*/*dV* curves exhibit symmetric behavior. For the *I-V* curve, under the same magnitude of the bias voltage, the current intensity of 0 ° TBGNRJ is smaller than 60 ° TBGNRJ for all voltages. For the *dI*/*dV* curves, the value of 60 ° TBGNRJ is higher than 0 ° TBGNRJ from -0.6 *V* to 0.6 *V*. However, 60 ° TBGNRJ is lower than 0 ° TBGNRJ at the rest voltages. More interestingly, the *I-V* and *dI*/*dV* curves demonstrate NDR in 21.8 ° and 38.2 ° rotation angles under ± 0.2 *V* bias voltage, which is mainly caused by transmission spectra under different bias voltages [46-48]. Although the calculated NDR is rather small, the NDR effect linked with the bias voltage was proposed in a prior research [49]. The physical reason of the NDR can be explained by analyzing the relationship between the transmission spectra and the applied bias voltage. Taking the 21.8 ° rotation angle as an example, the transmission spectra are displayed for the bias voltages of 0.2 V, 0.4 V, 0.6 V, 0.8 V and 1.0 V in the Figure 4(e). Under the 0.2 V bias voltage, the bias window directly related to the bias voltage is defined by ±0.1 eV around the Fermi level. The current rises to about 1.7 μA, which is caused by a peak of transmission spectra within the bias window. At the bias voltages of 0.4 V and 0.6 V, although the bias window widens, the peak values of transmission spectra within the bias window decrease, which indicates a reduced electron transmission. This reflects to a clear reduction of the current from about 1.7 μA at 0.2 V to 0.07 μA at 0.6 V and results to a peak-to-valley ratio around 24.3. However, with the bias voltage higher than 0.6 V, the peak of transmission spectra within the bias window increases, and the current increases subsequently.

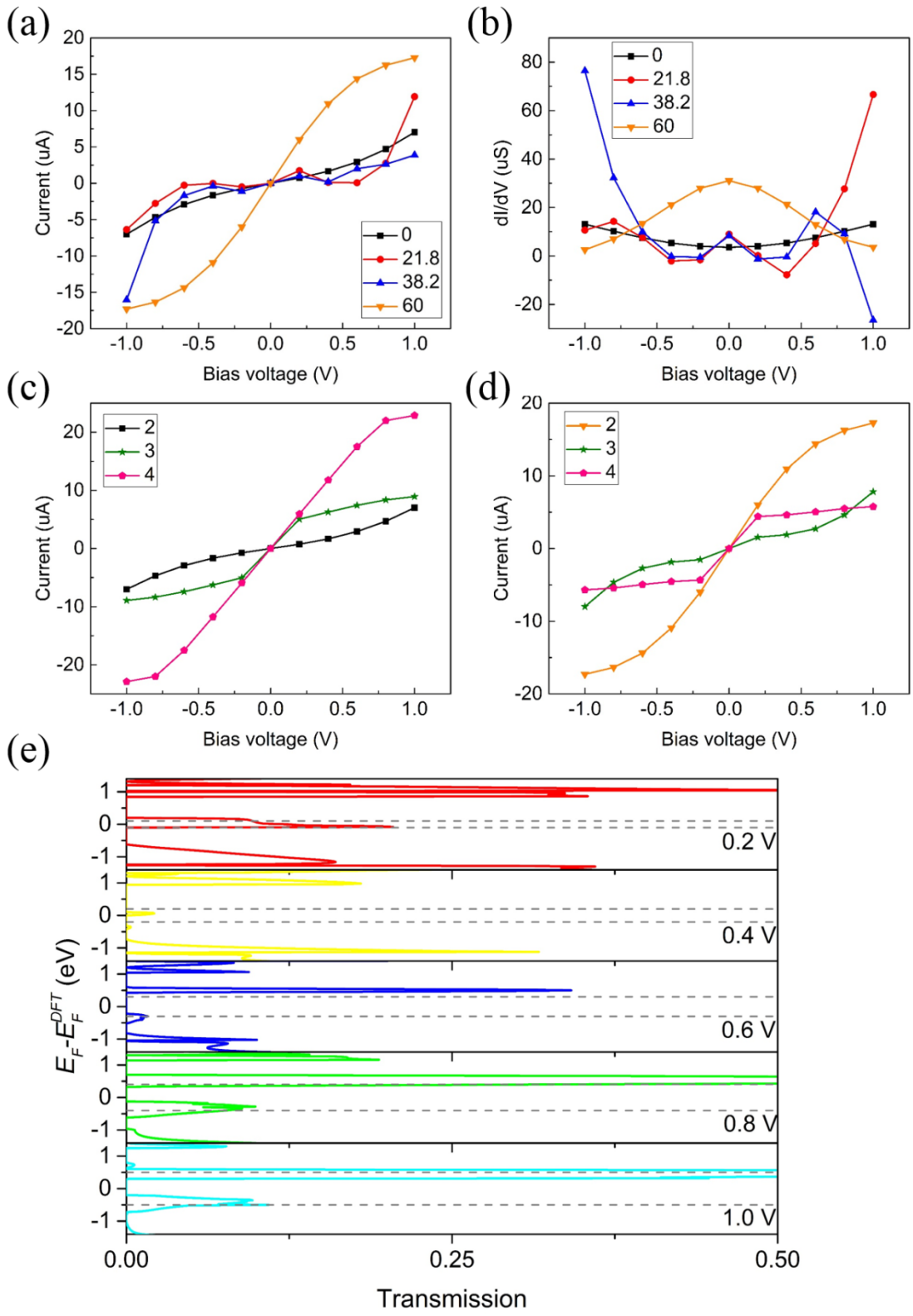

Figure 4. The I-V (a) and dI/dV (b) curves of the TBGNRJs with 0 º, 21.8 º, 38.2 º and 60 º rotation angles. (c) and (d) show the I-V with 0º and 60º TBGNRJs for 2, 3 and 4 graphene cells widths. (e) The electron transmission spectra of 21.8º TBGNRJ under 0.2 V, 0.4 V, 0.6 V, 0.8 V and 1.0 V bias voltages.

Thermoelectric properties of the TBGNRJs for the above twisting angles have also been simulated. Microscopically, the electron transport properties of the TBGNRJs can be described by the Boltzmann equation with the Fermi-Dirac distribution $f_{FD}(E,T)$. The electron conductance, Seebeck coefficient and heat transport coefficient of electrons are given by[50]:

$$G_e(T) = \frac{e^2}{h} L_0 \tag{5}$$

$$\mathrm{S(T)} = \frac{1}{eTL_0}\frac{L_1}{} \tag{6}$$

$$\kappa_e(T) = \frac{L_0 L_2 - L_1^2}{htL_0} \tag{7}$$

Where, e and h are the electron charge and Planck's constant.

$$L_n(T) = \int_{-\infty}^{+\infty} (E - E_F)^n T_e(E) \Big(- \frac{\partial f_{FD}(E,T)}{\partial E} \Big) dE \tag{8}$$

The heat transport coefficient of phonons is given by:

$$\kappa_{ph}(T) = \frac{1}{2\pi} \int_0^{\infty} \hbar w T_{ph}(\omega) \frac{\partial f_{BE}(\omega,T)}{\partial T} d\omega \tag{9}$$

Where, $f_{BE}(\omega, T)$ and $T_{ph}(\omega)$ are the Bose-Einstein distribution function and phonon transmission coefficient.

As shown in Figure 5, the electrical conductance, Seebeck coefficient, thermal conductance and *ZT* obtained in the TBGNRJs in the four twisting angles at 300 K are displayed. In the results, the chemical potential is a difference between the Fermi energy (E_F) and the DFT-predicted Fermi energy (E_F^{DFT}). The valleys and peaks of electrical conductance are shown in Figure 5(a) because of different band structures and bandgaps of the monolayer and bilayer parts of the TBGNRJs[20]. In Figure 5(b), the development of thermal conductance at four rotation angles have a similar trend with electrical conductance, which is similar to what is reported in the reference[15]. This result illustrates that the Seebeck coefficient is a key parameter to achieve high *ZT* value in the TGNRJs. In Figure 5(c), the maximum of Seebeck coefficient in 21.8 ^{o} and 38.2 ^{o} rotation angles is about 0.75 mV/K, which is about 7.5 times higher than the pristine graphene (~0.1 mV/K)[5, 51]. Figure 5(d) shows the *ZT* values of four TBNGRJs, four peak *ZT* values are more than 1 for the 21.8 ^{o} and 38.2 ^{o} rotation angles at 300 K. Particularly, in the 21.8 ^{o} rotation angle, the maximum *ZT* is 6.1, which is higher than most reported *ZT* values at room temperature[10, 52-54].

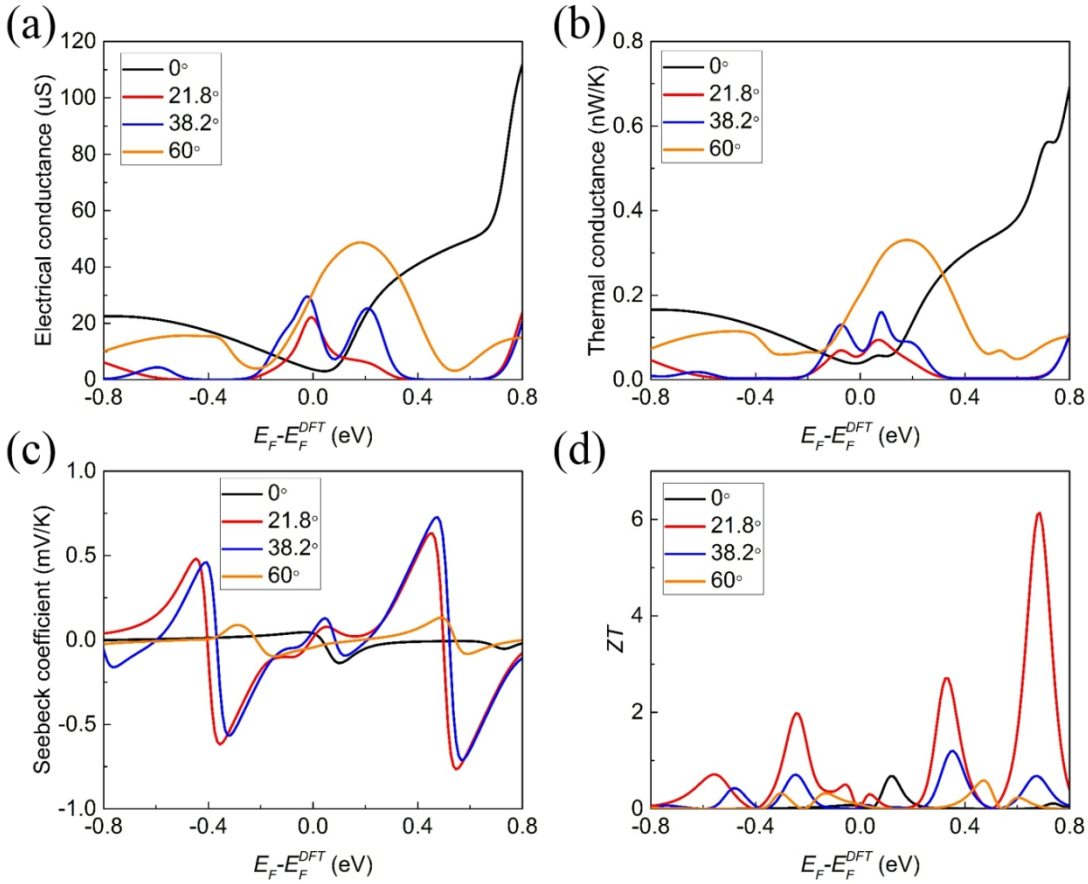

Figure 5. The electrical conductance (a), thermal conductance (b), Seebeck coefficient (c) and ZT (d) obtained in the TBGNRJs with 0 °, 21.8 °, 38.2 ° and 60 ° rotation angles at 300 K.

To summarize, band structures calculated in Figure 2 are from twisted bilayer graphene cells in Figure 1. Whereas the band structures in Figure 6 are for nanoribbon structures with hydrogen passivation shown in red dotted boxes in Figure 3. In our simulation, the twisted bilayer graphene nanoribbon is periodic along the *z*-direction. Comparing with the twisted bilayer graphene cells (Figure 1), all the carbon atoms at the edges of the twisted bilayer graphene nanoribbon are passivated by hydrogen atoms and a vacuum layer of 25 Å is added along the *x*-direction. These modelling processes break the symmetry of original twisted bilayer graphene cells, thus inducing significant band structure differences between the angles 0° and 60° (21.8° and 38.2°). The band structures of the four bilayer graphene nanoribbons along the Brillouin path through *Γ*-*Z* because the Seebeck coefficient is derived from the bandgap [55]. Bandgap opening is shown following the twisting of the bilayer graphene nanoribbons, which results in an increase of the Seebeck coefficient [56]. As shown in Figures 6(b) and (c), the bandgaps of the 21.8 ° and 38.2 ° TBGNRJs are 0.15 eV and 0.14 eV, which are larger than the bandgaps of 0 ° (0.02 eV) and 60.0 ° (0.11 eV) rotation angles. However, the bandgap opening of the 0 ° TBGNRJ is lower than the 25 meV (thermal fluctuation) at 300K, which is too small and tends to vanish in experiments.

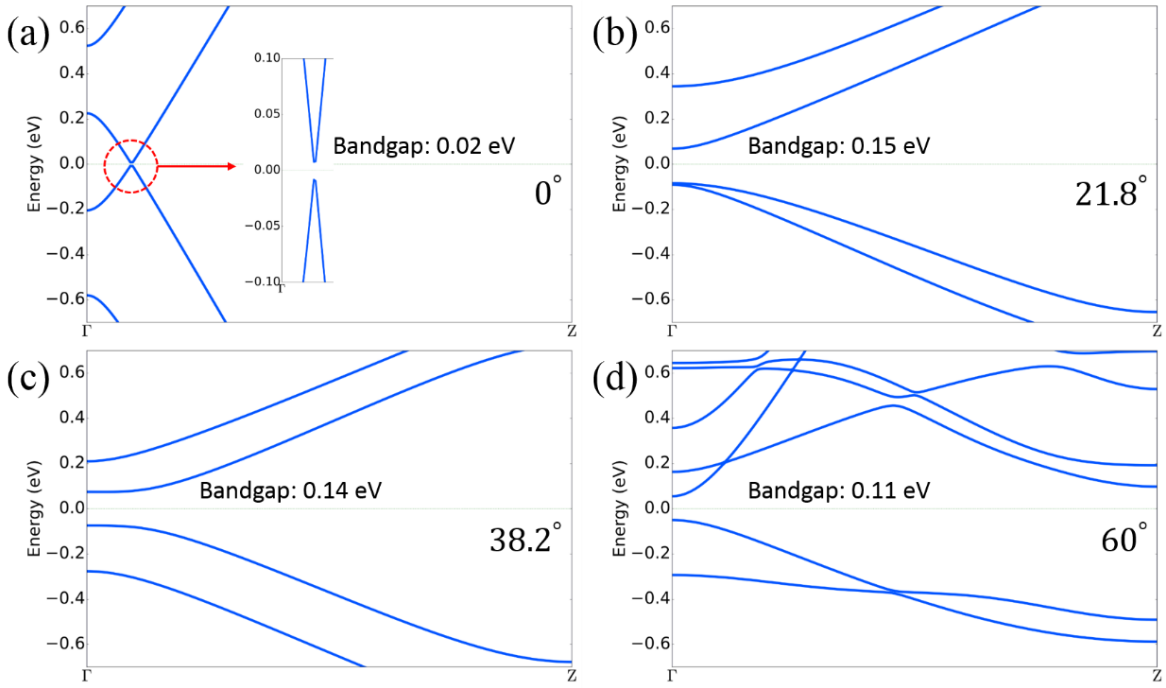

Figure 6. The computed band structures of the twisted bilayer graphene nanoribbons with 0 º (a) 21.8 º (b), 38.2 º (c) and 60 º (d) rotation angles.

Figure 5 (a) and Figure 7 (a) clearly show that an electrical conductance and transmission spectra gap in the range [0.3 – 0.7 eV] observed for the 21.8 º and 38.2 º TBGNRJs, which is hypothesized to be the cause of a high Seebeck coefficient. In the Figure 5 (c) and Figure 7 (a), the position of the Seebeck coefficient peak is consistent with the position of the electrical conductance and transmission spectra gap (0.3 eV-0.7 eV), which matches with the reference [57]. For 21.8° and 38.2° TBGNRJs, a clear transmission peak near the Fermi energy is due to the band bending and edge states, which has been described in prior theoretical and experimental research [58-60]. In the 21.8° and 38.2° TBGNRJs, a transmission spectra gap observed in the transmission spectra within the energy range from 0.3 eV to 0.7 eV, which is not observed in the 0° and 60° TBGNRJs. It is known that the transmission spectra and electrical conductance gap can improve the Seebeck coefficient and thermoelectric performance [61, 62]. In our case, the transmission spectra and electrical conductance gaps are due to the special twisting angles between two graphene nanoribbons, which affect the electrons transport through the interface of the top and bottom of the bilayer. Because there is no such transmission spectra and electrical conductance gap with rotation angles 0° and 60°, the Seebeck coefficient and *ZT* remain very small in these structures. To summary, we analyzed the electrical conductance and thermal conductance for 21.8° and 38.2° TBGNRJs in a 0.2 eV energy range consisting of the *ZT* peak. As shown in Figure 7 (c) and (d), the main reason of the high *ZT* is that at 21.8° and 38.2° angles, TBGNRJ exhibits a very small thermal conductivity (*K*) with small variations along the energy axis, and a relatively large electric conductivity (G_e).

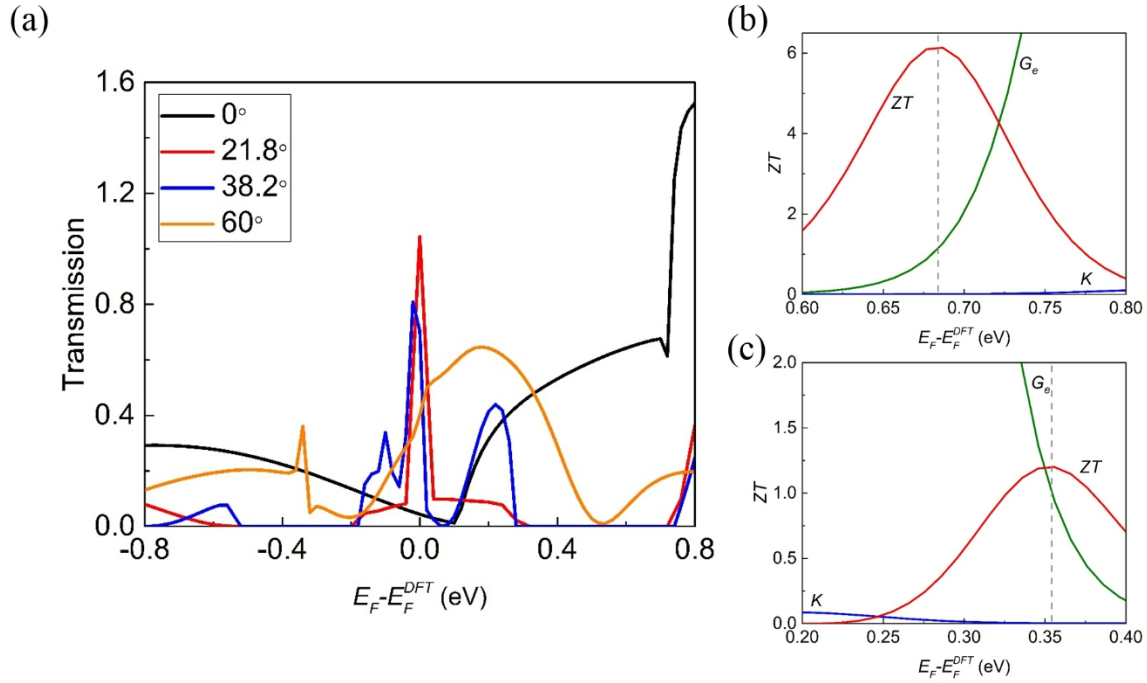

Figure 7. The electron transmission spectra obtained in the TBGNRJs at 300 K (a), the thermal conductance obtained in a single GNR of same width with the 0° TBGNRJ (b), electrical conductance, thermal conductance and ZT in the 0.2 eV energy range of the ZT peak with 21.8 º (c) and 38.2 º (d) TBGNRJs.

Figure 8 shows a comparison of the thermal conductance of the TBGNRJs (shown in Figure 5b) to that of a single GNR of same width. It is shown that there is a strong reduction of thermal conductance for the TBGNRJs compared with the single GNR. It is concluded that one of important contributions to the *ZT* enhancement of TBGNRJs should come from the strong reduction of thermal conductance. From Figure 5, the peaks of *ZT* higher than 1 exist in 21.8 º and 38.2 º rotation angles. We shall compute the thermal conductance of electrons and phonons for these TBGNRJs. As shown in Figure 9(a), the phonon contribution to the overall thermal conductance is much more than the electron contribution for *ZT* values of 2.7 and 2.0 in the 21.8 º TBGNRJs. However, at the *ZT* value of 6.1, the electron contribution to thermal conductance is comparable to that from the phonon. The maximum *ZT* value of 38.2 º TBGNRJs is 1.2, at which thermal conductance of electrons is slightly larger than that of phonons (Figure 9(c)). Figure 9(b) and (d) show that the thermal conductance of phonons increases with the rise of temperature. With all the electron and phonon transport properties calculated, we can evaluate the figure of merit of TBGNRJs. In Figure 5(d), all the outlines of *ZT* are rather asymmetric, and each of them has some peaks around the 0 eV. So, we can enhance *ZT* by appropriate *n*-type or *p*-type doping in these TBGNRJs at 300 K. For the 21.8 º rotation angles, there are three peak values of *ZT* ~ 2.0, 2.7 and 6.1 at around -0.25 eV, 0.33 eV and 0.68 eV, which means *n*-type doping are more favorable than *p*-type doping to improve the thermoelectric performance in the 21.8 º TBGNRJs. In the 38.2 º TBGNRJs, the maximum *ZT* value is 1.2 at 0.33 eV, which can be obtained by *n*-type doping. All these results suggest that 21.8 º TBGNRJs can obtain a significant improvement in thermoelectric performance at 300 K.

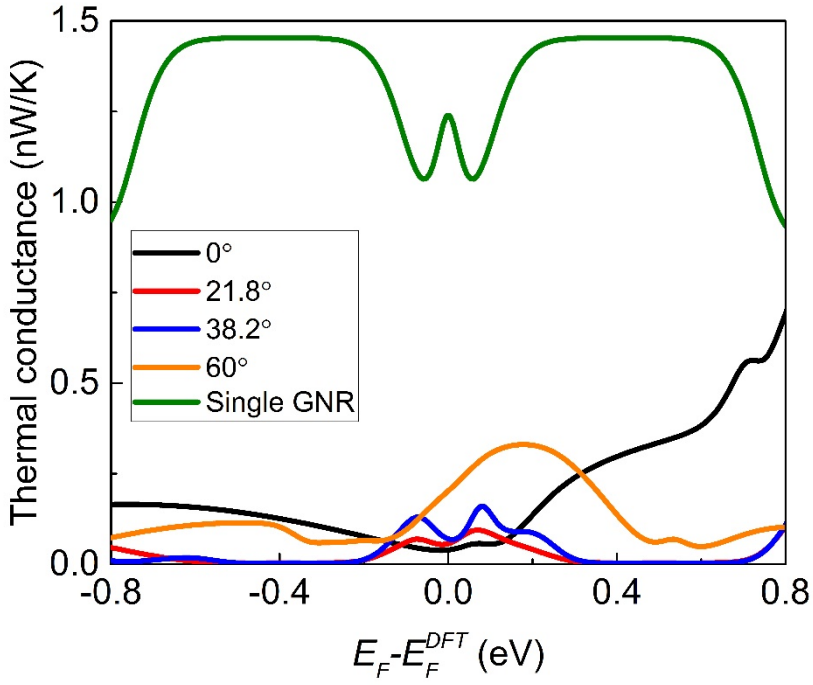

Figure 8. The thermal conductance obtained in a single GNR of same width with the TBGNRJs.

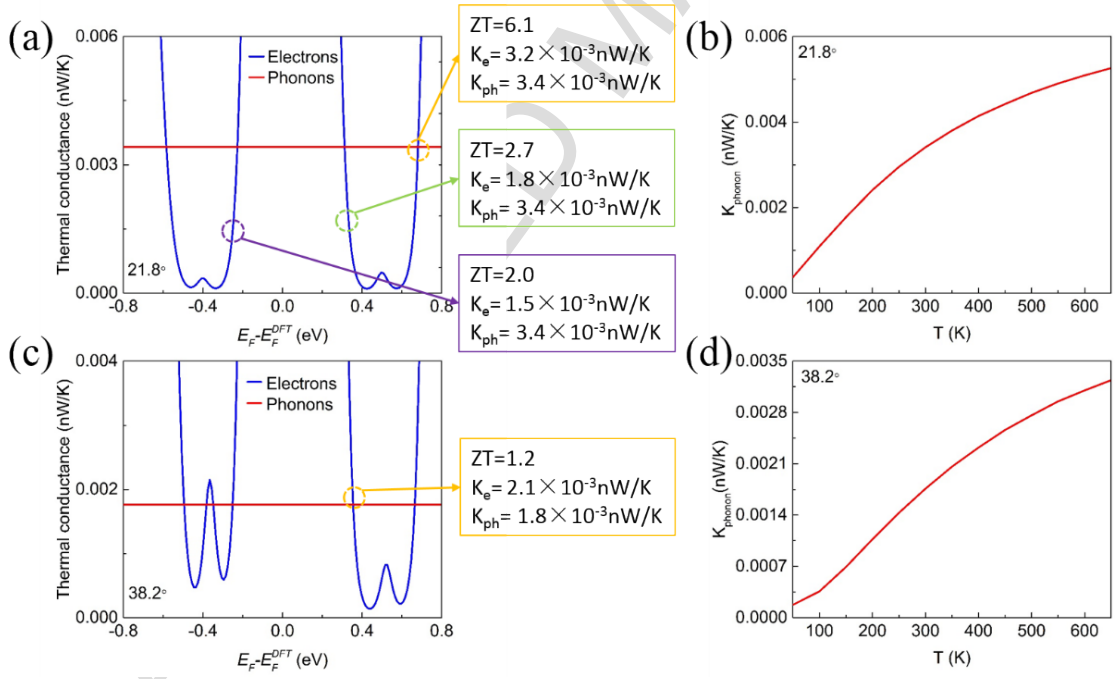

Figure 9. The electron and phonon contribution to the thermal conductance in 21.8 º (a) (b) and 38.2 º (c) (d) TBGNRJs.

4 Conclusion

We have investigated the electron transport and thermoelectric performance of TBGNRJs for 0 º, 21.8 º, 38.2 º and 60 º rotation angles by the first principles calculation. It is found that the

I-V curves of 0 °, 21.8 ° and 38.2 ° rotation angles exhibit behavior similar to p-n junctions. However, the 60 ° TBGNRJs is different, which exhibits an *I-V* curve similar to a transistor. NDR is shown in TBGNRJs at 21.8 ° and 38.2 ° rotation angles under ± 0.2 *V* bias voltage. High *ZT* values of 2.0, 2.7 and 6.1 have been achieved at -0.25 eV, 0.33 eV and 0.68 eV for the 21.8 ° rotation angles at 300K. It is interpreted that the reason of high *ZT* values of 21.8 ° TBGNRJ is due to its wider bandgap, transmission gap, electrical conduction gap and a strong reduction of thermal conductance for the TBGNRJs compared with the single GNR. Moreover, the phonon contribution to thermal conductance is much more than that of electrons in *ZT* values of 2.0 and 2.7 in the 21.8 ° TBGNRJs. At the *ZT* value of 6.1, the electron contribution to thermal conductance is comparable to that of phonons. The outstanding *ZT* values of TBGNRJs make it a promising device structure for thermoelectric applications.

Conflict of interest

There are no conflicts to declare.

Acknowledgements

Authors are grateful for funding by the China Scholarship Council (CSC). The authors would like to acknowledge the European Regional Development Fund (ERDF) for the funding of the Solar Photovoltaic Academic Research Consortium (SPARC II) which supported this research.

References

[1] K.S. Novoselov, A.K. Geim, S.V. Morozov, D. Jiang, Y. Zhang, S.V. Dubonos, I.V. Grigorieva, A.A. Firsov, Electric field effect in atomically thin carbon films, Science 306(5696) (2004) 666-669.

[2] K.I. Bolotin, K.J. Sikes, Z. Jiang, M. Klima, G. Fudenberg, J. Hone, P. Kim, H.L. Stormer, Ultrahigh electron mobility in suspended graphene, Solid State Commun. 146(9-10) (2008) 351-355.

[3] L. Banszerus, M. Schmitz, S. Engels, J. Dauber, M. Oellers, F. Haupt, K. Watanabe, T. Taniguchi, B. Beschoten, C. Stampfer, Ultrahigh-mobility graphene devices from chemical vapor deposition on reusable copper, Sci. Adv. 1(6) (2015).

[4] L. Banszerus, M. Schmitz, S. Engels, M. Goldsche, K. Watanabe, T. Taniguch, B. Beschoten, C. Stampfer, Ballistic Transport Exceeding 28 mu m in CVD Grown Graphene, Nano Lett. 16(2) (2016) 1387-1391.

[5] Y.M. Zuev, W. Chang, P. Kim, Thermoelectric and Magnetothermoelectric Transport Measurements of Graphene, Phys. Rev. Lett. 102(9) (2009).

[6] A.H. Castro Neto, F. Guinea, N.M.R. Peres, K.S. Novoselov, A.K. Geim, The electronic properties of graphene, Rev. Mod. Phys. 81(1) (2009) 109-162.

[7] A.A. Balandin, S. Ghosh, W.Z. Bao, I. Calizo, D. Teweldebrhan, F. Miao, C.N. Lau, Superior thermal conductivity of single-layer graphene, Nano Lett. 8(3) (2008) 902-907.

[8] K.S. Kim, Y. Zhao, H. Jang, S.Y. Lee, J.M. Kim, K.S. Kim, J.H. Ahn, P. Kim, J.Y. Choi, B.H. Hong, Large-scale pattern growth of graphene films for stretchable transparent electrodes, Nature 457(7230) (2009) 706-710.

[9] H. Jang, Y.J. Park, X. Chen, T. Das, M.S. Kim, J.H. Ahn, Graphene-Based Flexible and Stretchable Electronics, Adv. Mater. 28(22) (2016) 4184-4202.

[10] T.A. Amollo, G.T. Mola, M.S.K. Kirui, V.O. Nyamori, Graphene for Thermoelectric Applications: Prospects and Challenges, Crit. Rev. Solid State Mater. Sci. 43(2) (2018) 133-157.
[11] C.B. Vining, An inconvenient truth about thermoelectrics, Nat. Mater. 8(2) (2009) 83-85.
[12] Y. Xu, Z.Y. Li, W.H. Duan, Thermal and Thermoelectric Properties of Graphene, Small 10(11) (2014) 2182-2199.
[13] L.D. Hicks, M.S. Dresselhaus, Effect of Quantum-Well Structures on the Thermoelectric Figure of Merit, Phys. Rev. B 47(19) (1993) 12727-12731.
[14] L.D. Hicks, M.S. Dresselhaus, Thermoelectric Figure of Merit of a One-Dimensional Conductor, Phys. Rev. B 47(24) (1993) 16631-16634.
[15] H. Zheng, H.J. Liu, X.J. Tan, H.Y. Lv, L. Pan, J. Shi, X.F. Tang, Enhanced thermoelectric performance of graphene nanoribbons, Appl. Phys. Lett. 100(9) (2012).
[16] S.H. Tan, K.Q. Chen, The enhancement of the thermoelectric performance in zigzag graphene nanoribbon by edge states, Carbon 94 (2015) 942-945.
[17] L. Zhang, Z.Z. Yu, F.M. Xu, J. Wang, Influence of dephasing and B/N doping on valley Seebeck effect in zigzag graphene nanoribbons, Carbon 126 (2018) 183-189.
[18] Y.J. Ouyang, J. Guo, A theoretical study on thermoelectric properties of graphene nanoribbons, Appl. Phys. Lett. 94(26) (2009).
[19] H. Sevincli, C. Sevik, T. Cagin, G. Cuniberti, A bottom-up route to enhance thermoelectric figures of merit in graphene nanoribbons, Sci. Rep. 3 (2013).
[20] V.H. Nguyen, M.C. Nguyen, H.V. Nguyen, J. Saint-Martin, P. Dollfus, Enhanced thermoelectric figure of merit in vertical graphene junctions, Appl. Phys. Lett. 105(13) (2014).
[21] X.K. Gu, Y.J. Wei, X.B. Yin, B.W. Li, R.G. Yang, Colloquium: Phononic thermal properties of two-dimensional materials, Rev. Mod. Phys. 90(4) (2018).
[22] G. Pennelli, Review of nanostructured devices for thermoelectric applications, Beilstein J Nanotech 5 (2014) 1268-1284.
[23] B.L. Li, K.Q. Chen, Effects of electron-phonon interactions on the spin-dependent Seebeck effect in graphene nanoribbons, Carbon 119 (2017) 548-554.
[24] Z.Z. Yu, F.M. Xu, J. Wang, Valley Seebeck effect in gate tunable zigzag graphene nanoribbons, Carbon 99 (2016) 451-455.
[25] Z. Zhu, Z.G. Fthenakis, D. Tomanek, Electronic structure and transport in graphene/haeckelite hybrids: an ab initio study, 2d Materials 2(3) (2015).
[26] S.I. Vishkayi, M.B. Tagani, H.R. Soleimani, Enhancement of thermoelectric efficiency by embedding hexagonal boron-nitride cells in zigzag graphene nanoribbons, J Phys D Appl Phys 48(23) (2015).
[27] M.S. Hossain, F. Al-Dirini, F.M. Hossain, E. Skafidas, High Performance Graphene Nano-ribbon Thermoelectric Devices by Incorporation and Dimensional Tuning of Nanopores, Sci. Rep. 5 (2015).
[28] V.T. Tran, J. Saint-Martin, P. Dollfus, S. Volz, Optimizing the thermoelectric performance of graphene nano-ribbons without degrading the electronic properties, Sci. Rep. 7 (2017).
[29] Y. Anno, Y. Imakita, K. Takei, S. Akita, T. Arie, Enhancement of graphene thermoelectric performance through defect engineering, 2d Materials 4(2) (2017).
[30] W.W. Zhao, Y.L. Wang, Z.T. Wu, W.H. Wang, K.D. Bi, Z. Liang, J.K. Yang, Y.F. Chen, Z.P. Xu, Z.H. Ni, Defect-Engineered Heat Transport in Graphene: A Route to High Efficient Thermal Rectification, Sci. Rep. 5 (2015).

[31] Y. Cao, V. Fatemi, A. Demir, S. Fang, S.L. Tomarken, J.Y. Luo, J.D. Sanchez-Yamagishi, K. Watanabe, T. Taniguchi, E. Kaxiras, R.C. Ashoori, P. Jarillo-Herrero, Correlated insulator behaviour at half-filling in magic-angle graphene superlattices, Nature 556(7699) (2018) 80-+.
[32] S.J. Ahn, P. Moon, T.H. Kim, H.W. Kim, H.C. Shin, E.H. Kim, H.W. Cha, S.J. Kahng, P. Kim, M. Koshino, Y.W. Son, C.W. Yang, J.R. Ahn, Dirac electrons in a dodecagonal graphene quasicrystal, Science 361(6404) (2018) 782-+.
[33] W. Yao, E.Y. Wang, C.H. Bao, Y.O. Zhang, K.A. Zhang, K.J. Bao, C.K. Chan, C.Y. Chen, J. Avila, M.C. Asensio, J.Y. Zhu, S.Y. Zhou, Quasicrystalline 30 degrees twisted bilayer graphene as an incommensurate superlattice with strong interlayer coupling, Proc. Natl. Acad. Sci. U.S.A. 115(27) (2018) 6928-6933.
[34] Y. Cao, V. Fatemi, S. Fang, K. Watanabe, T. Taniguchi, E. Kaxiras, P. Jarillo-Herrero, Unconventional superconductivity in magic-angle graphene superlattices, Nature 556(7699) (2018) 43-+.
[35] M. Pelc, E.S. Morell, L. Brey, L. Chico, Electronic Conductance of Twisted Bilayer Nanoribbon Flakes, J. Phys. Chem. C 119(18) (2015) 10076-10084.
[36] L. Jelver, P.M. Larsen, D. Stradi, K. Stokbro, K.W. Jacobsen, Determination of low-strain interfaces via geometric matching, Phys. Rev. B 96(8) (2017).
[37] C.Y. Li, B. Debnath, X.J. Tan, S.S. Su, K. Xu, S.P. Ge, M.R. Neupane, R.K. Lake, Commensurate lattice constant dependent thermal conductivity of misoriented bilayer graphene, Carbon 138 (2018) 451-457.
[38] Atomistix ToolKit (ATK), https://quantumwise.com/. .
[39] S. Grimme, Semiempirical GGA-type density functional constructed with a long-range dispersion correction, J. Comput. Chem. 27(15) (2006) 1787-1799.
[40] A. Mohammadi, S. Haji-Nasiri, The electronic transport properties of defected bilayer sliding armchair graphene nanoribbons, Phys. Lett. A 382(15) (2018) 1040-1046.
[41] F. Gargiulo, O.V. Yazyev, Structural and electronic transformation in low-angle twisted bilayer graphene, 2d Materials 5(1) (2018).
[42] J.M.B.L. dos Santos, N.M.R. Peres, A.H. Castro, Graphene bilayer with a twist: Electronic structure, Phys. Rev. Lett. 99(25) (2007).
[43] N. Lu, H.Y. Guo, Z.W. Zhuo, L. Wang, X.J. Wu, X.C. Zeng, Twisted MX2/MoS2 heterobilayers: effect of van der Waals interaction on the electronic structure, Nanoscale 9(48) (2017) 19131-19138.
[44] M. Buttiker, Y. Imry, R. Landauer, S. Pinhas, Generalized Many-Channel Conductance Formula with Application to Small Rings, Phys. Rev. B 31(10) (1985) 6207-6215.
[45] Y.J. Li, M.D. Li, J.S. Liu, Q.Q. Sun, P. Zhou, P.F. Wang, S.J. Ding, D.W. Zhang, Atomic scale investigation of the abnormal transport properties in bilayer graphene nanoribbon, Appl. Phys. Lett. 100(1) (2012).
[46] K.M.M. Habib, S. Ahsan, R.K. Lake, Computational Study of Negative Differential Resistance in Graphene Bilayer Nanostructures, Proc Spie 8101 (2011).
[47] J. Kumar, H.B. Nemade, P.K. Giri, Density functional theory investigation of negative differential resistance and efficient spin filtering in niobium-doped armchair graphene nanoribbons, Phys. Chem. Chem. Phys. 19(43) (2017) 29685-29692.
[48] D. Zhang, M.Q. Long, X.J. Zhang, L.L. Cui, X.M. Li, H. Xu, Perfect spin filtering, rectifying

and negative differential resistance effects in armchair graphene nanoribbons, J. Appl. Phys. 121(9) (2017).
[49] S. Li, C.K. Gan, Y.W. Son, Y.P. Feng, S.Y. Quek, Low-bias negative differential resistance effect in armchair graphene nanoribbon junctions, Appl. Phys. Lett. 106(1) (2015).
[50] H. Sadeghi, S. Sangtarash, C.J. Lambert, Oligoyne Molecular Junctions for Efficient Room Temperature Thermoelectric Power Generation, Nano Lett. 15(11) (2015) 7467-7472.
[51] J.G. Checkelsky, N.P. Ong, Thermopower and Nernst effect in graphene in a magnetic field, Phys. Rev. B 80(8) (2009).
[52] H.L. Liu, X. Shi, F.F. Xu, L.L. Zhang, W.Q. Zhang, L.D. Chen, Q. Li, C. Uher, T. Day, G.J. Snyder, Copper ion liquid-like thermoelectrics, Nat. Mater. 11(5) (2012) 422-425.
[53] L. Han, D.V. Christensen, A. Bhowmik, S.B. Simonsen, L.T. Hung, E. Abdellahi, Y.Z. Chen, N.V. Nong, S. Linderoth, N. Pryds, Scandium-doped zinc cadmium oxide as a new stable n-type oxide thermoelectric material, J Mater Chem A 4(31) (2016) 12221-12231.
[54] R. Chetty, A. Bali, R.C. Mallik, Tetrahedrites as thermoelectric materials: an overview, J. Mater. Chem. C 3(48) (2015) 12364-12378.
[55] Y. Yokomizo, J. Nakamura, Giant Seebeck coefficient of the graphene/h-BN superlattices, Appl. Phys. Lett. 103(11) (2013).
[56] J.M. Zheng, P. Guo, Z.Y. Ren, Z.Y. Jiang, J.T. Bai, Z.Y. Zhang, Conductance fluctuations as a function of sliding motion in bilayer graphene nanoribbon junction: A first-principles investigation, Appl. Phys. Lett. 101(8) (2012).
[57] G.J. Snyder, E.S. Toberer, Complex thermoelectric materials, Nat. Mater. 7(2) (2008) 105-114.
[58] K. Nakada, M. Fujita, G. Dresselhaus, M.S. Dresselhaus, Edge state in graphene ribbons: Nanometer size effect and edge shape dependence, Phys. Rev. B 54(24) (1996) 17954-17961.
[59] X.T. Jia, M. Hofmann, V. Meunier, B.G. Sumpter, J. Campos-Delgado, J.M. Romo-Herrera, H.B. Son, Y.P. Hsieh, A. Reina, J. Kong, M. Terrones, M.S. Dresselhaus, Controlled Formation of Sharp Zigzag and Armchair Edges in Graphitic Nanoribbons, Science 323(5922) (2009) 1701-1705.
[60] J. Lahiri, Y. Lin, P. Bozkurt, I.I. Oleynik, M. Batzill, An extended defect in graphene as a metallic wire, Nat. Nanotechnol. 5(5) (2010) 326-329.
[61] H. Sadeghi, S. Sangtarash, C.J. Lambert, Enhanced Thermoelectric Efficiency of Porous Silicene Nanoribbons, Sci. Rep. 5 (2015).
[62] H. Sadeghi, S. Sangtarash, C.J. Lambert, Enhancing the thermoelectric figure of merit in engineered graphene nanoribbons, Beilstein J Nanotech 6 (2015) 1176-1182.

Enhanced thermoelectric performance of twisted bilayer graphene nanoribbons junction

Shuo Deng[1,2], Xiang Cai[2], Yan Zhang[3*], and Lijie Li[2*]
[1]School of Logistic Engineering, Wuhan University of Technology, Wuhan 430070
[2]College of Engineering, Swansea University, Swansea SA1 8EN
[3]School of Physics, University of Electronic Science and Technology of China, Chengdu 610054
*Emails: zhangyan@uest.edu.cn, L.Li@swansea.ac.uk